Medical Image Analysis 17 (2013) 892–906

Contents lists available at SciVerse ScienceDirect

Medical Image Analysis

journal homepage: www.elsevier.com/locate/media

Dynamic programming in parallel boundary detection with application to ultrasound intima-media segmentation

Yuan Zhou [a,*,1], Xinyao Cheng [b,1,2], Xiangyang Xu [a,3], Enmin Song [a,4]

[a] School of Computer Science and Technology, Huazhong University of Science and Technology, 1037 Luoyu Road, Wuhan, Hubei 430074, PR China
[b] Echocardiographic Laboratory of Cardiovascular Division, Department of Geriatrics, Zhongnan Hospital, Wuhan University, 169 Donghu Road, Wuhan, Hubei 430071, PR China

ARTICLE INFO

Article history:
Received 18 March 2012
Received in revised form 26 May 2013
Accepted 28 May 2013
Available online 6 June 2013

Keywords:
Parallel boundary detection
Intima-media thickness
Dual line detection
Dynamic programming
Optimization
Active contour model

ABSTRACT

Segmentation of carotid artery intima-media in longitudinal ultrasound images for measuring its thickness to predict cardiovascular diseases can be simplified as detecting two nearly parallel boundaries within a certain distance range, when plaque with irregular shapes is not considered. In this paper, we improve the implementation of two dynamic programming (DP) based approaches to parallel boundary detection, dual dynamic programming (DDP) and piecewise linear dual dynamic programming (PL-DDP). Then, a novel DP based approach, dual line detection (DLD), which translates the original 2-D curve position to a 4-D parameter space representing two line segments in a local image segment, is proposed to solve the problem while maintaining efficiency and rotation invariance. To apply the DLD to ultrasound intima-media segmentation, it is imbedded in a framework that employs an edge map obtained from multiplication of the responses of two edge detectors with different scales and a coupled snake model that simultaneously deforms the two contours for maintaining parallelism. The experimental results on synthetic images and carotid arteries of clinical ultrasound images indicate improved performance of the proposed DLD compared to DDP and PL-DDP, with respect to accuracy and efficiency.

© 2013 Elsevier B.V. All rights reserved.

1. Introduction

Boundary detection in longitudinal ultrasound carotid artery images has focused on automatic and accurate intima-media segmentation in the far wall for measurement of the thickness, which has been demonstrated to be an independent risk factor for cardiovascular disease (Bots et al., 1997; Lamont et al., 2000; O'Leary et al., 1999; Poredos, 2004). Fig. 1 illustrates three examples in which the intima-media complex (IMC) is a double-layered structure that features bright and dark bands enclosed by dark lumen above and bright adventitia below, whose boundary is defined by two parallel interfaces, the *lumen-intima* (LI) (upper boundary) and the *media-adventitia* (MA) (lower boundary). This is not an easy task because of the intrinsic variability of the intima-media structure and the extrinsic interference from the ultrasound machine. For anatomical variability, the thickness range demands consideration of all possible thicknesses while the boundary curve complicates an analytic representation. For common artifacts generated from the ultrasound machine, the interferences can be mainly categorized by strong noise in the lumen region and missing boundary in the intima layer (see Fig. 1). When plaque with significant local thickening exists, the situation could become more complex because its shape can differ greatly from the intima-media with a small thickness. Therefore, in this paper, we consider only intima-media with two nearly parallel boundaries as most of the previously proposed intima-media segmentation methods did (Cheng and Jiang, 2008; Destrempes et al., 2009; Loizou et al., 2007; Xu et al., 2012).

1.1. Previous research

There are a variety of segmentation algorithms proposed in this field, which were recently reviewed by Molinari et al. (Molinari et al., 2010). The employed techniques include dynamic programming (DP) (Cheng and Jiang, 2008; Liang et al., 2000; Wendelhag et al., 1997), active contour model (Cheng et al., 2002; Loizou

Abbreviations: CDLD, constrained dual line detection; DDP, dual dynamic programming; DLD, dual line detection; DP, dynamic programming; IMC, intima-media complex; IMT, intima-media thickness; LDLD, linked dual line detection; LI, Lumen-intima; MA, media-adventitia; MAD, mean absolute difference; PL-DDP, piecewise linear dual dynamic programming; SDP, single dynamic programming; UDLD, unconstrained dual line detection.

* Corresponding author. Present address: Building No.3, 99 Haike Road, Shanghai Advanced Research Institute, Chinese Academy of Sciences, Pudong, Shanghai, PR China. Tel.: +86 13818874384.

E-mail addresses: zhouyuanzxcv@gmail.com (Y. Zhou), xycheng@whu.edu.cn (X. Cheng), xuxy@hust.edu.cn (X. Xu), esong@mail.hust.edu.cn (E. Song).

[1] These authors contributed equally to this work.
[2] Tel.: +86 13971170236.
[3] Tel.: +86 13871009617.
[4] Tel.: +86 13871254332.

1361-8415/$ - see front matter © 2013 Elsevier B.V. All rights reserved.
http://dx.doi.org/10.1016/j.media.2013.05.009

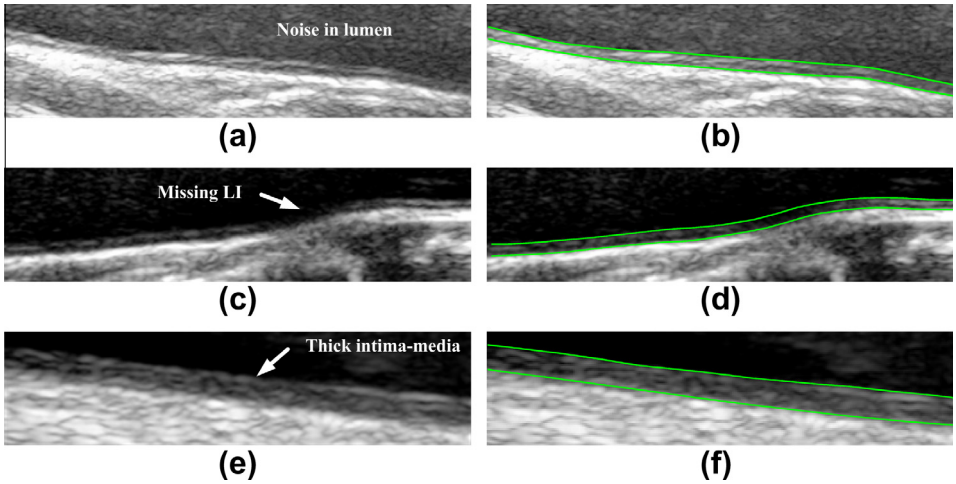

Fig. 1. Illustration of the intima-media in ultrasound carotid artery images, in which the IMC is a double-layered structure enclosed by dark lumen above and bright adventitia below. The left column shows original ROI images while the right column shows manually delineated boundary contours.

et al., 2007; Xu et al., 2012), stochastic optimization. (Destrempes et al., 2009) and spline fitting (Rocha et al., 2010, 2011), among which the most natural algorithm regarding such tasks could be single dynamic programming (SDP) (Liang et al., 2000), as defined by minimizing the following cost function

$$C_{SDP}(y_1, y_2, \ldots, y_N) = \kappa \sum_{n=2}^{N} |y_{n-1} - y_n| - \sum_{n=1}^{N} f(n, y_n) \quad (1)$$

where y_n, $n = 1, 2, \ldots, N$ is the y-coordinate of the boundary point in the nth column, $f(x, y) : \Omega \to \mathbb{R}^+$ is an edge map that has large values near the boundary, $\Omega = \{(x, y) | 1 \leqslant x \leqslant N, 1 \leqslant y \leqslant M\}$ is the image plane of size $N \times M$ (let the origin of the coordinate system be the top left corner), and κ is a parameter that controls the smoothness of the detected boundary. The key of DP is to write (1) in a recursion form so that a cost map containing minimal intermediate costs can be constructed through *forward recursion*, and then, the optimal solution can be found through *back tracing* (Amini et al., 1990). Because the cost map has the same size of the image plane, in which each intermediate cost is computed by considering all the costs in the previous column, the time complexity of forward recursion is $O(NM^2)$. The back tracing traces back from the minimal cost of the last column to the first column in $O(N)$ to find the optimal path.

SDP is a simple approach for detecting one side boundary; thus, it was applied to intima-media segmentation quite early (Liang et al., 2000; Wendelhag et al., 1997). Because the boundary of intima-media can be defined by two nearly parallel interfaces without the presence of plaque, a more ideal approach for such a problem could consider two boundaries simultaneously in the cost function, which was later proposed as dual dynamic programming (DDP) (Cheng and Jiang, 2008). The DDP has been demonstrated to be superior to SDP by imposing a hard constraint relating to the distance range and a soft constraint relating to its variation, except that the large computational cost requires $O(NM^2)$ even through a fast implementation that considers only neighboring costs in the forward recursion (Cheng and Jiang, 2008).

There has been other research conducted for similar tasks, in which piecewise linear dual dynamic programming (PL-DDP) was proposed for spine boundary detection (Wei et al., 2001a,b). The PL-DDP partitions the image plane into several equal-width non-overlapping segments, in each of which two line segments controlled by their endpoints are used to approximate the local boundaries. Because the curve smoothness of PL-DDP is controlled by the hard constraints of the angles between adjacent line segments, the method benefits from having a rotation-invariant nature. However, due to the dimension of the cost map, the solution employed in (Wei et al., 2001a,b) has a very large computational cost, $O(NM^4)$. Although piecewise linear approximation is not accurate for intima-media segmentation, further refinement based on an active contour model can be applied thereafter.

Further generalization includes extending the DP based detection of two parallel boundaries to multiple paths. For example, reference (Sun and Appleton, 2005) constrained the smoothness of the path through hard constraints that forced the path points in adjacent columns to be within a certain range. Similar to DDP, multiple hard constraints relating to the properties between paths, such as the order and distance as well as the heuristic constraints that use local maxima in the edge map, were proposed to reduce the computational cost. A specific application of this generalization to detecting two boundaries of membrane was proposed later, which adopted a polar transform of the original image for the following DP (Sun et al., 2009).

The above DP methods have two characteristics that we need to mention here. First, except for PL-DDP, the curve smoothness is defined by the vertical distance between two adjacent boundary points (first order derivative), which is not rotation invariant. Thus, it is possible that a slanting boundary demands a small curve smoothness to maintain the slope of the two ends while a horizontal boundary demands a large curve smoothness to overcome noise. This leads to a complicated training procedure for choosing the optimal parameters (Cheng and Jiang, 2008; Liang et al., 2000), which might not be successfully applied to all the situations. Second, because the DP searches the whole image plane to detect the boundaries, the computational cost achieves $O(NM^2)$ for DDP and $O(NM^4)$ for PL-DDP. We will show, in Section 2, that they could achieve $O(NM)$ complexity via fast implementations. However, it is still not a trivial task when the image becomes large.

1.2. Our contribution

In this paper, we propose a novel algorithm that avoids the above shortcomings for parallel boundary detection and validate the method in the context of ultrasound LI and MA boundary tracing. The boundary curve is divided into several parts, each of which is approximated using a line segment that can be defined by two parameters using a polar representation. The endpoints of the adjacent parts are linked via minimization of their vertical distance. Geometric constraints such as the distance and the angle between the two line segments are also incorporated naturally. Several

remarks can be made about this representation. First, in each segment, because of the polar representation of the line, the hard constraints can be imposed in a rotation-invariant way. Second, when the length of a part is small enough to equal the width of a single column, the algorithm degrades to a DP which is similar to DDP. Third, when the length of the part is large enough to equal the width of the image plane, the algorithm degrades to line detection which is similar to finding peaks in the parameter space of the Hough transform. Hence, it benefits from the robustness of both the Hough transform and DP. Moreover, it overcomes the weakness of the Hough transform that requires a very high dimensional parameter space for complex curves and the inconsistent curve smoothness measure of the above DP. Finally, because the algorithm operates on the edge points instead of on the whole image plane, apart from the thresholding procedure to determine the edge points, the remaining part could achieve linear time complexity $O(N)$.

The remainder of this paper is organized as follows. Section 2 reviews the previous DDP and PL-DDP, for which we suggest that, under certain hard constraints, the complexity of the solution can be reduced to $O(NM)$. Section 3 introduces the theoretical model of the proposed dual line detection (DLD) for parallel boundary detection and a fast solution that requires only $O(N)$. Section 4 proposes a framework to imbed the DLD for ultrasound intima-media segmentation, which includes three steps, as illustrated in Fig. 2. Then, after a description of data acquisition and algorithm implementation in Section 5, Section 6 presents and discusses comparative results on these methods. The final Section gives conclusive remarks.

2. Dynamic programming in parallel boundary detection

The problem of parallel boundary detection, regardless of whether it is in ultrasound intima-media segmentation or spine boundary detection, can be defined as finding two boundaries that have the following features:

1. The boundary of either side should be a smooth curve (intra-curve smoothness).
2. The two side boundaries should be nearly parallel (inter-curve smoothness) and have a distance within a specific range.

Suppose that the edge map $f(x, y)$ is given by an edge detector; then, the objective of parallel boundary detection becomes finding two curves that satisfy the above two constraints while passing through large values in $f(x, y)$. Following this definition, two approaches, DDP and PL-DDP, which include two curves in the cost function and solve for the optimal solution through DP, are discussed in this Section.

2.1. Dual dynamic programming

The DDP is defined by minimizing a combined cost function of (1)

$$C_{DDP}(\mathbf{y}_1, \mathbf{y}_2, \ldots, \mathbf{y}_N) = \kappa_1 \sum_{n=2}^{N} |d_{n-1} - d_n| + \kappa_2 \sum_{n=2}^{N} \|\mathbf{y}_{n-1} - \mathbf{y}_n\| - \sum_{n=1}^{N} \sum_{i=1}^{2} f(n, y_{n,i}) \quad (2)$$

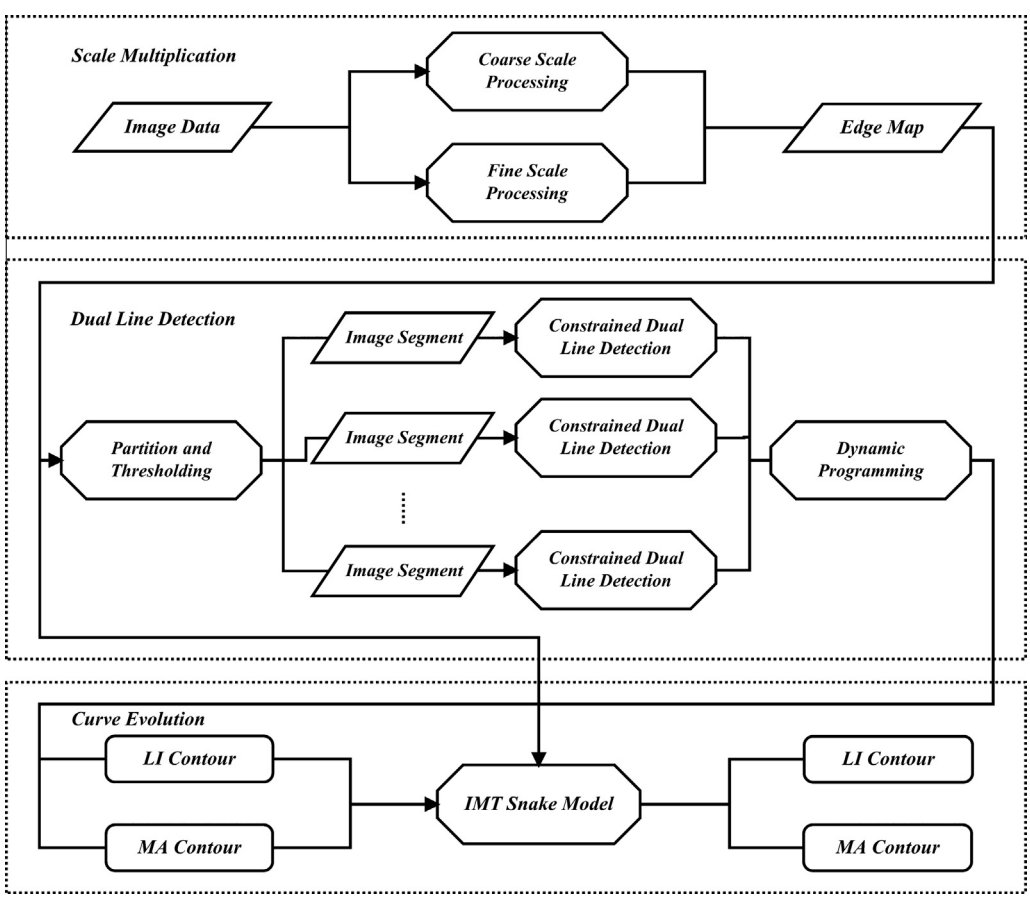

Fig. 2. Overview of the proposed intima-media segmentation approach.

subject to

$$d_{\min} \leqslant d_n \leqslant d_{\max}$$

where $\mathbf{y}_n = (y_{n,1}, y_{n,2})^T$ denotes the boundary points of LI ($y_{n,1}$) and MA ($y_{n,2}$) in the nth column, $\|\cdot\|$ denotes norm of the vector (L1-norm in (Cheng and Jiang, 2008)), $d_n = y_{n,2} - y_{n,1}$ is the distance between two boundary points which is constrained by the range [$d_{\min}$, $d_{\max}$], and κ_1 controls the uniformity of the distance (inter-curve smoothness) between the two boundary curves, while κ_2 controls their intra-curve smoothness. The recursion form of (2) can be written as

$$\begin{cases} C'_{DDP}(\mathbf{y}_n) = \min\limits_{\mathbf{y}_{n-1}}\{C'_{DDP}(\mathbf{y}_{n-1}) + \kappa_1|d_{n-1} - d_n| + \kappa_2\|\mathbf{y}_{n-1} - \mathbf{y}_n\|\} - \sum\limits_{i=1}^{2} f(n, y_{n,i}) \\ C'_{DDP}(\mathbf{y}_1) = -\sum\limits_{i=1}^{2} f(1, y_{1,i}) \end{cases} \tag{3}$$

where $C'_{DDP}(\mathbf{y}_n) = \min_{\mathbf{y}_1,\mathbf{y}_2,\ldots,\mathbf{y}_{n-1}} C_{DDP}(\mathbf{y}_1, \mathbf{y}_2, \ldots, \mathbf{y}_n)$ is the minimal cost ending at $\mathbf{y}_n$, $n = 2, 3, \ldots, N$.

The computation of $C'_{DDP}(\mathbf{y}_n)$ can be constrained by $d_{\min} \leqslant d_n \leqslant d_{\max}$, and the possible $\mathbf{y}_{n-1}$ for each computation can be limited to 9 neighbors centered around $\mathbf{y}_n$; thus, the complexity of the forward recursion can be reduced to $O(NM)$. Fig. 3a illustrates this process in the construction of the cost map. Note that the original memory cost of DDP requires $O(NM^2)$ for the cost map, which makes the method inapplicable for large images. However, if we store only values that satisfy $d_{\min} \leqslant d_n \leqslant d_{\max}$ (see the shadowed area in Fig. 3a), the memory cost can also be reduced to $O(NM)$.

2.2. Piecewise linear dual dynamic programming

The original PL-DDP is intended to detect vertical spine boundaries and contains some constraints with similar smoothing effects. Here, we modify the method for horizontal boundary detection and keep a minimal set of hard constraints to derive a simplified version. To be specific, we partition the edge map $f(x, y)$ horizontally into S equal-width non-overlapping segments $\{f_s(x, y)|s = 1, 2, \ldots, S\}$, where $1 \leqslant x \leqslant N_s$, $1 \leqslant y \leqslant M$, approximate the local two-sided boundaries using line segments $L_s = \{l_{s,1}, l_{s,2}\}$, $s = 1, 2, \ldots, S$, which are controlled by endpoints (y-coordinates) $\mathbf{e}_{s-1}$ and $\mathbf{e}_s$, where $\mathbf{e}_s = (e_{s,1}, e_{s,2})^T$, $s = 0, 1, \ldots, S$, and find a set of line segments $\{L_s|s = 1, 2, \ldots, S\}$ that pass through strong edges as many as possible by minimizing the following cost function

$$C_{PL-DDP}(\mathbf{e}_0, \mathbf{e}_1, \ldots, \mathbf{e}_S) = -\sum_{s=1}^{S}\sum_{i=1}^{2} f_s(l_{s,i}) \tag{4}$$

where

$$f_s(l_{s,i}) = \sum_{n=1}^{N_s} f_s(n, (n/N_s)e_{s,i} + (1 - n/N_s)e_{s-1,i})$$

subject to

$$\begin{aligned} &\theta_{\min} \leqslant \theta_{s,i} \leqslant \theta_{\max} \\ &\angle(l_{s,1}, l_{s,2}) \leqslant \omega_1 \\ &\angle(l_{s,i}, l_{s-1,i}) \leqslant \omega_2 \\ &d_{\min} \leqslant e_{s,2} - e_{s,1} \leqslant d_{\max} \end{aligned}$$

where $\angle(.,.)$ denotes the angle between two line segments, $\theta_{s,i}$ is the angle between $l_{s,i}$ and the horizontal axis, $\theta_{\min}$, $\theta_{\max}$ constrain the line segment to be within a certain orientation range, ω_1, ω_2 control the inter-curve smoothness and intra-curve smoothness, respectively, and $d_{\min}$, $d_{\max}$ specify the range of the distance. The recursion form of (4) can be written as

$$\begin{cases} C'_{PL-DDP}(\mathbf{e}_s) = \min\limits_{\mathbf{e}_{s-1}}\left\{C'_{PL-DDP}(\mathbf{e}_{s-1}) - \sum\limits_{i=1}^{2} f_s(l_{s,i})\right\} \\ C'_{PL-DDP}(\mathbf{e}_0) = 0 \end{cases} \tag{5}$$

where $C'_{PL-DDP}(\mathbf{e}_s) = \min_{\mathbf{e}_0,\mathbf{e}_1,\ldots,\mathbf{e}_{s-1}} C_{PL-DDP}(\mathbf{e}_0, \mathbf{e}_1, \ldots, \mathbf{e}_s)$ is the minimal cost ending at $\mathbf{e}_s$, $s = 1, 2, \ldots, S$.

Although the forward recursion requires every $\mathbf{e}_{s-1}$ for each computation at $\mathbf{e}_s$, the hard constraints imply that both of them can be constrained to a certain range. First, we observe that $d_{\min} \leqslant e_{s,2} - e_{s,1} \leqslant d_{\max}$ constrains $\mathbf{e}_s$ in a narrow band similar to the DDP. Second, $\theta_{\min} \leqslant \theta_{s,i} \leqslant \theta_{\max}$ implies that $N_s \tan\theta_{\min} \leqslant |e_{s-1,i} - e_{s,i}| \leqslant N_s \tan\theta_{\max}$, which can be used to constrain the possible values of $\mathbf{e}_{s-1}$ for computation. Fig. 3b illustrates these constraints in the construction of the cost map. Note that, although the theoretical cost is reduced to $O(NM)$, because the wide range of $[N_s \tan\theta_{\min}, N_s \tan\theta_{\max}]$ leads to many evaluations of $f_s(l_{s,i})$ and calculations of the orientation of the two line segments for comparison with ω_1 and ω_2, the actual time cost is still large.

3. Dual line detection

We reviewed two examples of parallel boundary detection, DDP and PL-DDP, in the above Section, where two fast implementations that exploit multiple hard constraints and reduce the computational costs to $O(NM)$ were discussed. However, we also see that because of their nature that relies on the whole image plane, without further constraints, such a cost is a minimum requirement. Here, we propose a novel DP that approximates the parallel

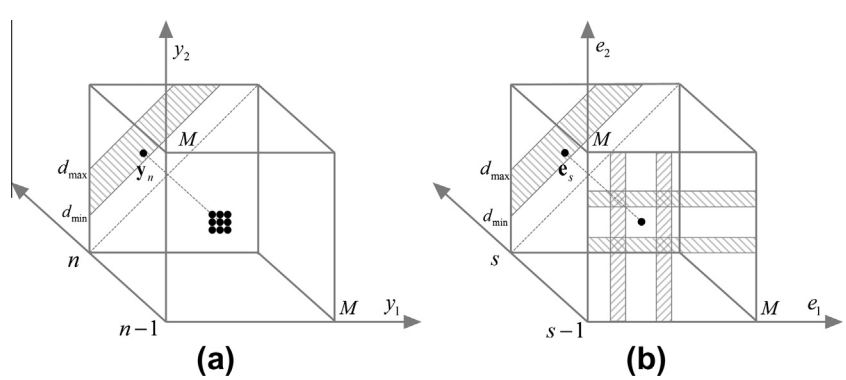

Fig. 3. The forward recursion of DDP (a) and PL-DDP (b). (a) The shadowed area indicates the constrained computation of $C'_{DDP}(\mathbf{y}_n)$ via $d_{\min} \leqslant d_n \leqslant d_{\max}$, which relies on 9 neighbors in the previous page. (b) Through imposing hard constraints, both in the evaluation of $\mathbf{e}_s$ (shadowed band in the sth page via $d_{\min} \leqslant e_{s,2} - e_{s,1} \leqslant d_{\max}$) and in the selection of $\mathbf{e}_{s-1}$ (double shadowed rectangles in the $(s-1)$th page via $\theta_{\min} \leqslant \theta_{s,i} \leqslant \theta_{\max}$), the computational cost can be reduced to $O(NM)$.

boundaries via piecewise linear representation, which not only is rotation invariant but also *could* achieve linear time complexity.

3.1. Theory

The DLD partitions the edge map horizontally into equal-width non-overlapping segments and approximates the local boundaries using parallel line segments. Inspired by (Toronto et al., 2007), we adopt a Bayesian variation of the Hough transform in each segment so that multiple lines can be extracted with shape constraints imposed. The Hough transform, as a special case of the Radon transform (Deans, 1981), represents a line by two parameters ρ and θ, where ρ denotes the distance between the line and the origin of the image plane and θ denotes the orientation of the line so that, given an arbitrary point (x, y) that belongs to the line, equation (6) is satisfied (Duda and Hart, 1972).

$$\rho = x\cos\theta + y\sin\theta \tag{6}$$

Suppose that, in an edge map $f(x, y)$,K edge points $X = \{(x_1, y_1), (x_2, y_2), \ldots, (x_K, y_K)\}$ that have non-zero values exist. We aim to extract a set of two lines $L = \{l_1, l_2\}$ from these edge points, where each l_i can be represented by a parameter pair (ρ_i, θ_i). Based on the analysis in (Toronto et al., 2007), we define the conditional probability density of the edge point (x_k, y_k) given line l_i, $i = 1, 2$ by

$$P(x_k, y_k|l_i) \propto \exp(\delta(x_k\cos\theta_i + y_k\sin\theta_i - \rho_i)) \tag{7}$$

where $\delta(z)$ is a regularized Dirac delta function that is close to one when z is close to zero and is close to zero otherwise. Note that $|x_k \cos\theta_i + y_k \sin\theta_i - \rho_i|$ is the distance between point (x_k, y_k) and the line specified by (ρ_i, θ_i), so the probability achieves its maximum when the line passes through (x_k, y_k). This definition originates from the assumption that the edge points are mainly generated by the boundary (the line segment used to approximate the boundary). Furthermore, we can also assume that the larger $f(x_k, y_k)$ is, the more likely (x_k, y_k) is to be an edge point, i.e., the probability in (7) can be modified by

$$P(x_k, y_k|f, l_i) \propto \exp(f(x_k, y_k)\delta(x_k\cos\theta_i + y_k\sin\theta_i - \rho_i)) \tag{8}$$

Since we have a set of non-overlapping line segments that approximate boundaries, each edge point could be generated by one line segment. The conditional probability density of the edge point (x_k, y_k), given a set of two lines L, can be naturally defined by

$$P(x_k, y_k|f, L) \propto \max\{P(x_k, y_k|f, l_1), P(x_k, y_k|f, l_2)\} \tag{9}$$

Considering that each edge point satisfies an independent distribution, the probability of all the edge points is the product of the independent components.

$$P(X|f, L) = \prod_{k=1}^{K} P(x_k, y_k|f, L) \tag{10}$$

The definition of parallel boundary detection implies that the local detected line segments should be nearly parallel and their distance satisfies a predefined range. We can assume that their angle and distance satisfy Gaussian distributions and define a prior probability of a line set by

$$\begin{aligned} &P(L) = P(l_1, l_2) = P(\rho_1, \theta_1, \rho_2, \theta_2) = P(\rho_1, \rho_2)P(\theta_1, \theta_2) \\ &P(\rho_1, \rho_2) = \exp(-(\rho_2 - \rho_1 - \eta)^2/2\gamma^2) \\ &P(\theta_1, \theta_2) = \exp(-(\theta_2 - \theta_1)^2/2\omega^2) \end{aligned} \tag{11}$$

where η is the desired distance between two line segments, and γ specifies the variation range of the distances centered at η. The parameter ω specifies the variation range for the angle between two line segments as approximately 0. Note that here we assume the variables ρ_i and θ_i are independent because they are two parameters to represent the line without correlation. Using Bayesian theory, the posterior probability of the line set given the edge points can be derived by

$$P(L|f, X) \propto P(X|f, L)P(L) \tag{12}$$

if $P(X) = \prod_{k=1}^{K} P(x_k, y_k)$ is a constant by assuming that the probability of edge point $P(x_k, y_k)$ satisfies a uniform distribution.

The objective of finding two parallel line segments becomes the same as maximizing the posterior of the line set given all the edge points in the edge map.

$$L^* = \arg\max_L P(L|f, X) \tag{13}$$

Combining Eqs. (8)–(12), maximizing $P(L|f, X)$ is equivalent to maximizing

$$\begin{aligned} D(\boldsymbol{\theta}) &= \log P(L|f, X) \\ &= \underbrace{\sum_{k=1}^{K} f(x_k, y_k)\max\{\delta(x_k\cos\theta_i + y_k\sin\theta_i - \rho_i)|i = 1, 2\}}_{\text{line matching}} \\ &\quad \underbrace{-\frac{(\rho_2 - \rho_1 - \eta)^2}{2\gamma^2} - \frac{(\theta_2 - \theta_1)^2}{2\omega^2}}_{\text{shape constraint}} \end{aligned} \tag{14}$$

where $\boldsymbol{\theta} = (\theta_1, \theta_2, \rho_1, \rho_2)^T$ specifies the two line segments. Note that the line-matching term is similar to the accumulator array that is constructed by using the Hough transform (suppose $f(x_k, y_k) = 1$ and $i = 1$; then, it degrades to the Hough transform for line detection). We refer to this problem as unconstrained dual line detection (UDLD).

The shape constraint in (14) can be imposed on the optimization problem as a hard constraint through assuming a uniform distribution for the line set, which transforms the objective to maximizing

$$D(\boldsymbol{\theta}) = \sum_{k=1}^{K} f(x_k, y_k)\max\{\delta(x_k\cos\theta_i + y_k\sin\theta_i - \rho_i)|i = 1, 2\} \tag{15}$$

subject to

$$\begin{aligned} &-\omega_1 \leqslant \theta_2 - \theta_1 \leqslant \omega_1 \\ &d_{\min} \leqslant \rho_2 - \rho_1 \leqslant d_{\max} \end{aligned}$$

We refer to the above problem as constrained dual line detection (CDLD). Eq. (15) has an intuitive interpretation that each edge point belonging to the line set contributes its strength to the objective function. The Gaussian distribution $G_{\mu,\sigma}(x)$ has a large probability in the interval $[\mu - 3\sigma, \mu + 3\sigma]$; thus, we can assume that the prior probability $P(L)$ constrains the solution of UDLD in $\{\boldsymbol{\theta}|\eta - 3\gamma \leqslant \rho_2 - \rho_1 \leqslant \eta + 3\gamma, -3\omega \leqslant \theta_2 - \theta_1 \leqslant 3\omega\}$, which makes the UDLD similar to CDLD except for the additional term of the shape constraint.

Suppose that the partition of the edge map $f(x, y)$ provides S equal-width non-overlapping image segments denoted by $\{f_s(x, y)|s = 1, 2, \ldots, S\}$ for each $f_s(x, y)$, $1 \leqslant x \leqslant N_s$ having two line segments $L_s = \{l_{s,1}, l_{s,2}\}$ corresponding to the local boundaries, where $l_{s,i}$, $i = 1, 2$ can be represented by a parameter pair $(\rho_{s,i}, \theta_{s,i})$. The piecewise linear approximation for two parallel boundaries can be obtained by maximizing

$$U(\boldsymbol{\theta}_1, \boldsymbol{\theta}_2, \ldots, \boldsymbol{\theta}_S) = \sum_{s=1}^{S} D_s(\boldsymbol{\theta}_s) \tag{16}$$

where $\boldsymbol{\theta}_s = (\theta_{s,1}, \theta_{s,2}, \rho_{s,1}, \rho_{s,2})^T$ and D_s is the UDLD or CDLD of f_s.

Although $D_s(\boldsymbol{\theta}_s)$ guarantees that the detected line segments are optimal with respect to the edge points in the image segment, such an optimization is localized and no neighboring information is considered. Similar to DDP and PL-DDP, two neighboring

constraints can be imposed here. First, we can assume that the adjacent line segments belonging to the same interface have a maximal angle, i.e., $-\omega_2 \leqslant \theta_{s,i} - \theta_{s-1,i} \leqslant \omega_2$. Second, we can ensure that their adjacent endpoints be closely linked by minimizing a function $G(\boldsymbol{\theta}_{s-1}, \boldsymbol{\theta}_s)$ that measures the distance between the endpoints

$$G(\boldsymbol{\theta}_{s-1}, \boldsymbol{\theta}_s) = \|\mathbf{e}_{s-1,R} - \mathbf{e}_{s,L}\| \tag{17}$$

where $\mathbf{e}_{s,L}$ ($\mathbf{e}_{s,R}$) are the y-coordinates of the two left (right) endpoints of the line segment pair specified by $\boldsymbol{\theta}_s$. The notation $\|\cdot\|$ represents any type of valid norm, and we chose the L1-norm for simplicity.

Combining local line detection and adjacent linkage, we propose a linked dual line detection (LDLD) that makes the two line segments in each image segment pass through the edge points as many as possible, while linking to their respective neighbors, by minimizing

$$U(\boldsymbol{\theta}_1, \boldsymbol{\theta}_2, \ldots, \boldsymbol{\theta}_S) = \lambda \sum_{s=2}^{S} G(\boldsymbol{\theta}_{s-1}, \boldsymbol{\theta}_s) - \sum_{s=1}^{S} D_s(\boldsymbol{\theta}_s) \tag{18}$$

subject to

$$\begin{aligned} &-\omega_1 \leqslant \theta_{s,2} - \theta_{s,1} \leqslant \omega_1 \\ &-\omega_2 \leqslant \theta_{s,i} - \theta_{s-1,i} \leqslant \omega_2 \\ &d_{\min} \leqslant \rho_{s,2} - \rho_{s,1} \leqslant d_{\max} \end{aligned}$$

where D_s adopts the form in (15), and λ is a positive that controls how close the adjacent endpoints should be. Fig. 4 illustrates this representation of two parallel boundaries given artificial edge points. Eq. (18) involves $4S$ parameters. If each one is discretized by H values, minimizing (18) would have H^{4S} possible solutions. Common optimization approaches, such as simulated annealing, Nelder-Mead Simplex and Markov Chain Monte Carlo (Spall, 2003), might either have a slow convergence rate or be attracted to local minima. We use a two-step algorithm to solve the problem. The first step calculates the non-zero values D_s ($\boldsymbol{\theta}_s$) of the 4-D discretized parameter space for each image segment. The second step uses DP to find $\{\boldsymbol{\theta}_s | s = 1, 2, \ldots, S\}$ of those non-zero values that minimize $U(\boldsymbol{\theta}_1, \boldsymbol{\theta}_2, \ldots, \boldsymbol{\theta}_S)$.

3.2. Solution

To solve the problem of LDLD by a 4-D DP, the focus shifts to efficiently evaluating $D_s(\boldsymbol{\theta}_s)$ in an image segment. Hence, we first discuss the solution of CDLD. Given an edge map of size $N \times M$, according to the requirement of LDLD that the endpoints of a line segment should lie at the left and right side boundary, Eq. (6) yields $\rho \in (0, M]$ when $\theta \in [0, \pi)$. Suppose that each parameter is discretized by H values; then, the 4-D parameter space $\{\boldsymbol{\theta} | 0 \leqslant \theta_i < \pi, 0 < \rho_i \leqslant M\}$ for CDLD can be divided into H^4 elements, where each element has a uniform size and is initialized to zero.

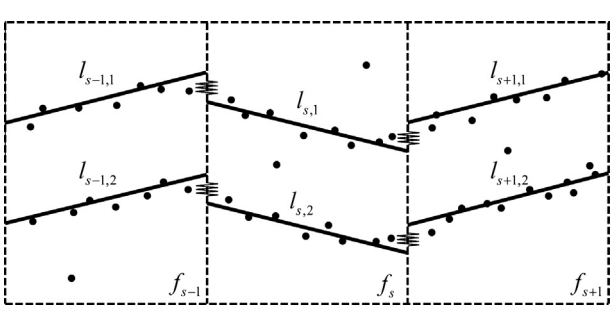

Fig. 4. Illustration of the proposed LDLD given a set of edge points. The line segments are attracted by the edge points while maintaining a spring that connects the endpoints of adjacent segments.

We now focus on Eq. (15), which contributes to an element sum of strengths of all the edge points passed through by the line set specified by the element. For a specific point (x_k, y_k) and a parameter pair (θ_1, θ_2), Eq. (15) suggests that, only when $x_k \cos\theta_i + y_k \sin\theta_i - \rho_i$ is near to zero, the edge strength $f(x_k, y_k)$ can be added to an element. Thus, we can solve $x_k \cos\theta_i + y_k \sin\theta_i - \rho_i = 0$ for ρ_i given (x_k, y_k) and θ_i, and then, we can add $f(x_k, y_k)$ to all the elements determined by $(\theta_1, \theta_2, \rho_i)$. Because the calculated ρ_i might not exactly correspond to a discrete value, round-off is needed in this step. Note that either of the two conditions $\{x_k \cos\theta_i + y_k \sin\theta_i - \rho_i = 0 | i = 1, 2\}$ holding would be sufficient to apply the above addition because the max{.,.} operation requires only one large $\delta(z)$; thus, the computation in the parameter space (ρ_1, ρ_2) given fixed (θ_1, θ_2) can be constrained into two strips that are determined by the calculated values of ρ_1 and ρ_2, resulting in a computational cost of $O(KH^3)$.

The key to our solution is to utilize the edge direction to constrain the selection of (θ_1, θ_2), similar to in (Ballard, 1981). For a specific edge point (x_k, y_k), the edge direction θ_0 can be calculated from the original image. Because the two lines to be extracted are more likely to generate an edge point with the same direction as one of them, the search for a maximum of (15) as well as the computation of (θ_1, θ_2) can be constrained in the vicinity of this direction. Note that the edge direction can be attributed to either of the two lines (here, we consider only the two side boundaries that have edge directions pointing to the same side, while the algorithm can be naturally extended to adapt to opposite sides); thus, again the computation of (θ_1, θ_2) can be constrained into two strips $\bigcup_{i=1,2}\{(\theta_1, \theta_2) | \theta_0 - \theta_\varepsilon \leqslant \theta_i \leqslant \theta_0 + \theta_\varepsilon\}$, where θ_ε is a small value that controls the size of the vicinity. The incorporation of the edge direction reduces the computational cost to $O(KH^2)$ for UDLD, whose solution can be obtained by adding the shape constraint in (14) to each of the non-zero values of (15).

Although the above solution is efficient for a 4-D optimization problem, the hard constraints in (15) can further reduce the complexity of CDLD to $O(K)$. To understand how they work, we first observe the angle constraint $-\omega_1 \leqslant \theta_2 - \theta_1 \leqslant \omega_1$, which constrains the selection of (θ_1, θ_2) into two narrow strips of length $2\omega_1$ determined by the edge direction. Then, the distance constraint $d_{\min} \leqslant \rho_2 - \rho_1 \leqslant d_{\max}$ further constrains the computation of (ρ_1, ρ_2) into strips of length $d_{\max} - d_{\min}$ determined by (θ_1, θ_2).

The above analysis is illustrated in Fig. 5, where the 4-D parameter space is decomposed by two 2-D spaces ((θ_1, θ_2) and (ρ_1, ρ_2)), and the shadowed areas indicate the elements that are required for the computation. Here, we give an example for an edge point with the direction θ_0. The edge point could be passed through by the line (ρ_1, θ_1), which means that we need to calculate all the elements at $\{(\theta_1, \theta_2) | \theta_1 = \theta_0, |\theta_2 - \theta_1| \leqslant \omega_1\}$, which corresponds to the horizontal shadowed strip in Fig. 5a. For (ρ_1, ρ_2) given each (θ_1, θ_2) in this strip, ρ_1 can be determined by $\rho_1 = x_k \cos\theta_1 + y_k \sin\theta_1$ because we assume that the edge point is passed through by the line (ρ_1, θ_1) in the first step. Suppose that the calculated ρ_1 equals ρ_0; then, given the hard constraint $d_{\min} \leqslant \rho_2 - \rho_1 \leqslant d_{\max}$, the calculation for (ρ_1, ρ_2) is constrained in the horizontal shadowed strip in Fig. 5c. Similar explanations can be deduced for Fig. 5b and d.

Accompanying the illustration, the pseudocode for CDLD is given in Fig. 6, where the 4-D sparse matrix can be implemented by using data structures such as red–black tree, hash table or trie, which contains a maximum of $\frac{8\theta_\varepsilon\omega_1(d_{\max}-d_{\min})}{\Delta\theta^2\Delta\rho}$ elements. Note that Figs. 5 and 6 apply to the detection of two side boundaries with edge directions that point to the same side, e.g., both LI and MA have edge directions that point downward. If the objective is to detect boundaries with edge directions that point to opposite sides,

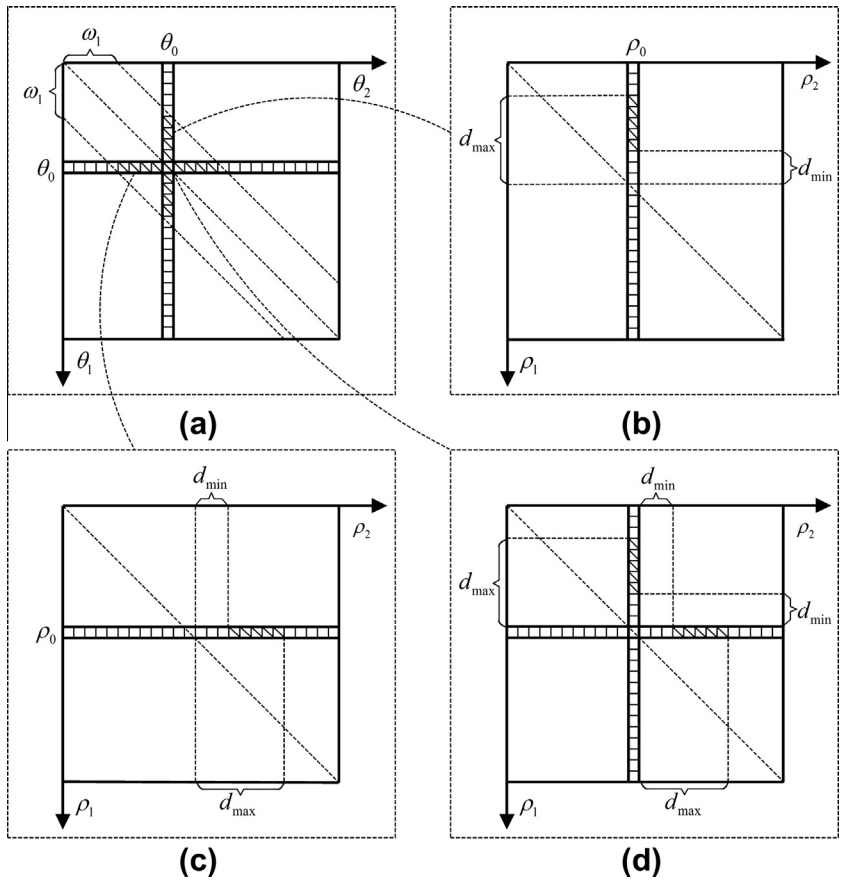

Fig. 5. Illustration of our solution, which exploits the edge direction and hard constraints for CDLD. (a) is the space of (θ_1, θ_2), where the computation can be first constrained into two strips that are crossed according to the edge direction θ_0 and further constrained into the shadowed area via $-\omega_1 \leqslant \theta_2 - \theta_1 \leqslant \omega_1$. (b) shows that, when $(\theta_1, \theta_2) \in \{(\theta_1, \theta_2) | \theta_2 = \theta_0, |\theta_2 - \theta_1| \leqslant \omega_1, \theta_2 \neq \theta_1\}$, the computation in the space of (ρ_1, ρ_2) can be constrained into a strip of length $d_{\max} - d_{\min}$ at $\rho_2 = \rho_0$, where $\rho_0 = x_k \cos\theta_0 + y_k \sin\theta_0$. (c) shows the constrained computation when $(\theta_1, \theta_2) \in \{(\theta_1, \theta_2) | \theta_1 = \theta_0, |\theta_2 - \theta_1| \leqslant \omega_1, \theta_2 \neq \theta_1\}$. (d) shows that, when $(\theta_1, \theta_2) \in \{(\theta_1, \theta_2) | \theta_1 = \theta_2 = \theta_0\}$, the computation is constrained into two strips, which means that either of the two lines can pass through this edge point since both of them match the edge direction now.

then the situation becomes somewhat simpler (only one strip in Fig. 5a) because the edge direction can help attribute the edge point to one side boundary.

Since the above solution for CDLD provides an efficient way to compute the non-zero values in $D_s(\boldsymbol{\theta}_s)$, we can solve the LDLD by selecting these values through DP. Although this approach excludes the possibility that zero values of $D_s(\boldsymbol{\theta}_s)$ may constitute an optimal solution, considering that such a case implies that none of the two lines in an image segment passes through any edge point, it is still acceptable in practical applications. Re-writing (18) into a recursion form, the DP can be defined by

$$\begin{cases} U'(\boldsymbol{\theta}_s) = \min\limits_{\boldsymbol{\theta}_{s-1}} \{U'(\boldsymbol{\theta}_{s-1}) + \lambda G(\boldsymbol{\theta}_{s-1}, \boldsymbol{\theta}_s)\} - D_s(\boldsymbol{\theta}_s) \\ U'(\boldsymbol{\theta}_1) = -D_1(\boldsymbol{\theta}_1) \end{cases} \tag{19}$$

where $U'(\boldsymbol{\theta}_s) = \min_{\boldsymbol{\theta}_1, \boldsymbol{\theta}_2, \ldots, \boldsymbol{\theta}_{s-1}} U(\boldsymbol{\theta}_1, \boldsymbol{\theta}_2, \ldots, \boldsymbol{\theta}_s)$ is the minimal cost ending at $\boldsymbol{\theta}_s$, $s = 2, 3, \ldots, S$. Because our solution has embedded the hard constraints relating to an image segment in $D_s(\boldsymbol{\theta}_s)$, the DP here only needs to consider $-\omega_2 \leqslant \theta_{s,i} - \theta_{s-1,i} \leqslant \omega_2$, which is easy to calculate due to our representation of line segments and can also reduce the computation in some situations.

To analyze the time complexity of this solution, we can assume that the edge map possesses K edge points, which are equally scattered in each image segment. According to the above analysis of CDLD, we need $O(\frac{K}{S} \cdot S)$ to build the 4-D parameter space for all the segments. Because the add operation in each segment occurs $O(\frac{K}{S})$ times, the number of non-zero elements should be less than $O(\frac{K}{S})$. Therefore, the worst case for the complexity of DP is $O(\frac{K}{S} \cdot \frac{K}{S} \cdot (S-1))$. Then, if we assume that the width of an image segment is a constant ($O(S) = O(N)$) and the number of edge points is proportional to the image width ($O(K) = O(N)$), the cost can be simplified to $O(N)$. Note that a similar analysis and result can be deduced for the requirement of memory.

4. Application to ultrasound intima-media segmentation

Segmentation of carotid artery intima-media in longitudinal ultrasound images is a huge challenge in medical imaging due to its low imaging quality. Because of the morphologic variability of plaque, most previous research has focused on segmentation in the carotid arteries without significant local thickening. In this paper, the problem is also restricted to carotid arteries with two nearly parallel boundaries. The application of the proposed DLD to ultrasound intima-media segmentation requires supplements of an edge map computation and a curve refinement. Here, we define the edge map by the product of the responses from edge detectors with different scales, and deform the initial contours from the DLD by a special snake model for accurate segmentation (see Fig. 2).

4.1. Scale multiplication

The edge map is usually defined by the gradient magnitude of the original image that highlights the boundary of the object to be segmented. However, when we identify the IMC, as illustrated

Algorithm for Constrained Dual Line Detection

Inputs: $\omega_1, d_{\min}, d_{\max}, f(x,y)$; **Outputs**: $\theta_1^*, \theta_2^*, \rho_1^*, \rho_2^*$

Initialize 4-D sparse matrix $D(\theta_1, \theta_2, \rho_1, \rho_2)$

For each edge point (x_k, y_k) for which $f(x_k, y_k) > \varepsilon$ holds **do**

Calculate the edge direction θ_0 of the edge point (x_k, y_k)

Approximate θ_0 to a nearest discrete angle

For θ_1 from $\theta_0 - \theta_\varepsilon$ to $\theta_0 + \theta_\varepsilon$ with step $\Delta\theta$ **do**

$\rho_1 \leftarrow x_k \cos\theta_1 + y_k \sin\theta_1$

Approximate ρ_1 to a nearest discrete distance

For θ_2 from $\theta_1 - \omega_1$ to $\theta_1 + \omega_1$ with step $\Delta\theta$ **do**

For ρ_2 from $\rho_1 + d_{\min}$ to $\rho_1 + d_{\max}$ with step $\Delta\rho$ **do**

Increase $D(\theta_1, \theta_2, \rho_1, \rho_2)$ by $f(x_k, y_k)$

For θ_2 from $\theta_0 - \theta_\varepsilon$ to $\theta_0 + \theta_\varepsilon$ with step $\Delta\theta$ **do**

$\rho_2 \leftarrow x_k \cos\theta_2 + y_k \sin\theta_2$

Approximate ρ_2 to a nearest discrete distance

For θ_1 from $\theta_2 - \omega_1$ to $\theta_2 + \omega_1$ with step $\Delta\theta$ **do**

For ρ_1 from $\rho_2 - d_{\max}$ to $\rho_2 - d_{\min}$ with step $\Delta\rho$ **do**

Increase $D(\theta_1, \theta_2, \rho_1, \rho_2)$ by $f(x_k, y_k)$

$(\theta_1^*, \theta_2^*, \rho_1^*, \rho_2^*) \leftarrow \arg\max D(\theta_1, \theta_2, \rho_1, \rho_2)$

Fig. 6. Pseudocode of algorithm for CDLD.

in Fig. 1, noise in the lumen region, the intima-media interface and the adventitia layer all create misleading edges, which would compromise the results of DLD and the subsequent curve evolution. To reduce their interference, we select only positive step edges with respect to the y-axis in the edge map by defining

$$f(x,y) = \max\left\{0, \frac{\partial G_\sigma}{\partial y} * I(x,y)\right\} \tag{20}$$

where $I(x, y)$ denotes the original ROI image, $G_\sigma(x,y) = \frac{1}{2\pi\sigma^2} e^{-(x^2+y^2)/2\sigma^2}$ is a 2-D Gaussian with a standard deviation of σ, $*$ denotes a convolution operation and $\frac{\partial}{\partial y}$ denotes the derivative with respect to y. This definition will remove the negative edges in the intima-media, as well as those in the lumen and adventitia layer.

The interference can be further reduced by using scale multiplication that defines the edge map by the product of the responses from two scale filters (Bao et al., 2005; Rosenfeld, 1970). The characteristics of ultrasound carotid artery images suggest that a sufficient coarse-scale could only keep the vessel wall while removing other fine features such as IMC (Liang et al., 2000). Thus, if an edge map from the coarse-scale image serves as an envelope of the fine-scale one, the edges can be localized near the IMC and the interference can be further reduced. Combining edge maps from different scales, the proposed edge map is defined by

$$f(x,y) = \prod_{i=1}^{2} \max\left\{0, \frac{\partial G_{\sigma_1}}{\partial y} * I(x,y)\right\} \tag{21}$$

where $G_{\sigma_1}(x,y)$ is a 2-D Gaussian with a small scale σ_1, and $G_{\sigma_2}(y) = \frac{1}{\sqrt{2\pi}\sigma_2} e^{-y^2/2\sigma_2^2}$ is a 1-D Gaussian with a large scale σ_2 to avoid the expensive 2-D convolution cost. The same directional edge scheme is used in the coarse-scale image since the artery wall also features positive step edges along the y-axis. Fig. 7 shows the benefits of this type of definition for reducing noise edges in the lumen and adventitia.

4.2. Dual line detection

Based on the edge map that was obtained from the scale multiplication, the proposed LDLD is applied here as an initial approximation to the boundary. Specifically, we determine the number of image segments by $S = \lceil N/l_{\max} \rceil$, where $l_{\max}$ controls the maximal width that a segment can achieve. Then, after independent normalization to 0–1 of each image segment, it is thresholded by a global constant ε to determine the local edge points. Finally, the cost function (18) is minimized through evaluating $D_s(\boldsymbol{\theta}_s)$ in each image segment and selecting the optimal line segments as two initial contours for the following active contour model.

The CDLD with edge directions and a thickness range taken from clinical images is important for this application. The key in this step is to construct a sparse matrix and to add values to some of its elements. We use a hash map to store its non-zero values, where the 4-D coordinate is transformed to a large index that is based on the size of the matrix; thus, modulo a prime can be used as the hash function. To reduce the computation of the following DP, a threshold t_m maxD_s ($\boldsymbol{\theta}_s$), where $0 < t_m < 1$, can be applied to

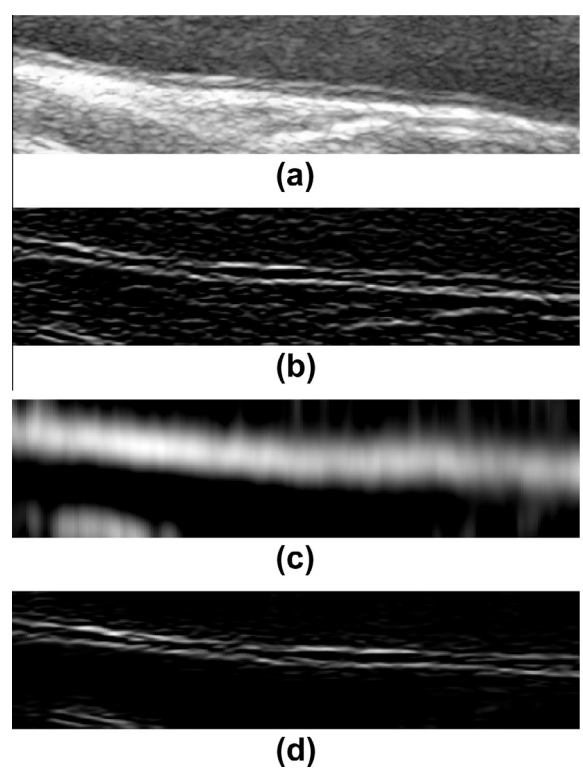

Fig. 7. Edge map obtained from scale multiplication for Fig. 1a. (a) Original image. (b) Edge map from a directional edge detector with a small scale ($\sigma_1 = 1$). (c) Edge map from a directional edge detector with a large scale ($\sigma_2 = 15$). (d) Combination of (b) and (c), resulting in an edge map that contains edges from the LI and MA while being free from edges that are away from the IMC.

eliminate its small values, which should correspond to the line sets that pass through only a few edge points. Because the edge map contains noise that leads to many small non-zero values in the matrix, this operation could save a substantial amount of actual time cost.

4.3. Curve evolution

The initial contours are inaccurate approximations to the desired boundaries. We choose snake model for accurate segmentation (Kass et al., 1988). Given the edge map $f(x,y):\Omega \to \mathbb{R}^+$, snake model drives a contour toward local maxima in $f(x, y)$ by defining a parametric curve $\Gamma(q)$:[0, 1] $\to \Omega$ that locally minimizes the energy functional

$$E(\Gamma) = \frac{\alpha}{2}\int \left\|\frac{\partial \Gamma}{\partial q}\right\|^2 dq + \frac{\beta}{2}\int \left\|\frac{\partial^2 \Gamma}{\partial q^2}\right\|^2 dq - \int f(\Gamma)dq \tag{22}$$

where $\Gamma(q) = (x(q),y(q))$, $\|\cdot\|$ denotes the L2-norm, $\frac{\partial \Gamma}{\partial q}$ and $\frac{\partial^2 \Gamma}{\partial q^2}$ denote the first and second derivatives of $\Gamma(q)$ with respect to q, and $x(q)$ and $y(q)$ are the x-coordinate and y-coordinate of the curve point $\Gamma(q)$. The parameters α and β control the weights of the curve length and the rigidity, both of which smooth the curve. Eq. (22) can be simplified for intima-media segmentation considering that the boundary curve can be represented by one y-coordinate per x-coordinate and that the first order smoothing term in (22) is sufficient to regularize the functional (Caselles et al., 1997). Therefore, we only need a miniature snake model that minimizes the following functional

$$E(y) = \frac{\alpha}{2}\int \left(\frac{\partial y}{\partial x}\right)^2 dx - \int f(x,y)dx \tag{23}$$

where $y(x)$: [1, N] $\to$ [1, M] denotes the boundary contour.

It is known that ultrasound segmentation could be hindered by the disappearance of boundary (Noble and Boukerroui, 2006), e.g., previous researchers proposed to handle it through incorporating shape priors from training data in heart and kidney segmentation (Chen et al., 2002; Xie et al., 2005). In the context of intima-media segmentation, the disappearance of boundary could result in two boundary curves being attracted to the same interface because the two side boundaries are rather close. Therefore, a shape constraint can be derived through reducing the distance variation between the two contours. Incorporating such a constraint into a variational framework, the proposed *IMT Snake model* is defined by minimizing

$$E(y_1,y_2) = \underbrace{\frac{1}{2}\sum_{i=1}^{2}\alpha_i \int \left(\frac{\partial y_i}{\partial x}\right)^2 dx}_{\text{smoothing energy}} - \underbrace{\sum_{i=1}^{2}\int f(x,y_i)dx}_{\text{boundary energy}} + \underbrace{\frac{\mu}{2}\int \left[\frac{\partial (y_2 - y_1)}{\partial x}\right]^2 dx}_{\text{uniform energy}} \tag{24}$$

where $y_1(x)$ and $y_2(x)$ denote the contours for LI and MA, respectively. We can see that, compared to (23), (24) added a uniform energy term that connects the independent contours together through forcing a uniform distance via parameter μ.

By gradient descent flow, minimizing (24) can be achieved by solving the partial differential equations (PDE)

$$\frac{\partial y_1}{\partial t} = \lambda_1 \frac{\partial^2 y_1}{\partial x^2} - \mu \frac{\partial^2 y_2}{\partial x^2} + \frac{\partial f}{\partial y}(x,y_1) \tag{25}$$

$$\frac{\partial y_2}{\partial t} = \lambda_2 \frac{\partial^2 y_2}{\partial x^2} - \mu \frac{\partial^2 y_1}{\partial x^2} + \frac{\partial f}{\partial y}(x,y_2) \tag{26}$$

where $\lambda_i = \alpha_i + \mu$, $i = 1, 2$ with the initial contours. The effect of uniform energy can be intuitively interpreted by separating $\mu\left(\frac{\partial^2 y_1}{\partial x^2} - \frac{\partial^2 y_2}{\partial x^2}\right)$ in (25) and considering it to be an adaptive spring that continuously attempts to maintain a uniform distance by pulling the curve point of the LI contour down when the distance of the current position is larger than its neighboring distances and vice versa. A similar interpretation for Eq. (26) can be deduced from a contrary movement of the MA contour. For the sake of stability, the numerical scheme (see the Appendix) for the right hand side employs implicit steps with respect to the first two terms and an explicit step with respect to the third term. Compared to the dual snake model in (Xu et al., 2012), the IMT Snake model is an improvement featuring fewer parameters and a stable iteration process.

5. Experimental setup

5.1. Data acquisition

In our experiments, all the clinical images were recorded from a Philips iE33 ultrasound system with an 11 MHz transducer in Zhongnan Hospital of Wuhan University, China, where the clinicians were allowed to adjust the gain setting and filter. We manually selected 200 images from 32 patients (22 male and 10 female, age 57 ± 20). For each image, a ROI was manually selected by choosing a rectangle that contains arteries displaying two nearly parallel boundaries, with IMT < 1.3 mm and without significant local thickening. The average ROI size is 19.0 × 5.5 mm, with a pixel spacing of 0.0665 mm. We also created a synthetic image containing two parallel boundaries with a distance of 12 pixels for efficiency evaluation, wherein each side boundary was defined by a sinusoid function. For each ROI, the two side boundaries were manually delineated 4 times in total by 2 clinical experts, to establish the gold standard via averaging the manual contours by interpolation. Consistent with the quantitative metric used in most of the related literature (Molinari et al., 2010), we defined the segmentation error by the mean absolute difference (MAD) of the interpolated curve points between the automatically generated contour and the gold standard contour (see Fig. 8 for the segmentation errors of LI, MA and IMC).

5.2. Parameter selection

The experiments were conducted on a personal computer with an Intel Core i5-430M processor and 4 GB memory. The programs were coded in MATLAB except for DDP, PL-DDP and LDLD, which were coded in C++ for optimal efficiency. We employed the same edge map from scale multiplication for all these algorithms, where

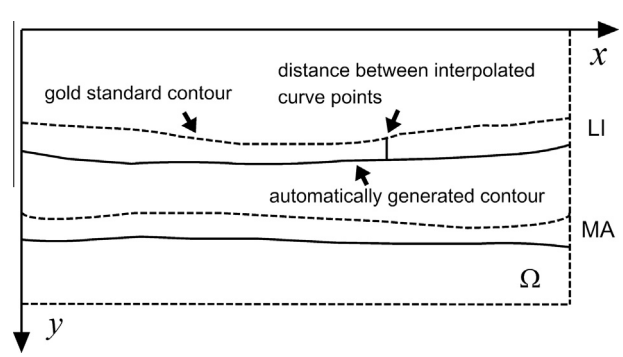

Fig. 8. The defined segmentation error (MAD) of LI, MA and IMC. The MAD of LI (MA) is the mean of the distances between the interpolated curve points from the gold standard contour and the automatically generated contour for the LI (MA) boundary. The MAD of IMC is the mean of all these distances.

Table 1
Optimal parameters trained for all the clinical images.

Parameter	DDP		PL-DDP	LDLD	
	κ_1	κ_2	$l_{\max}$	$l_{\max}$	λ
Without snake	1.60	0.16	50	30	4
With snake[a]	0.68	0.12	60	60	4

[a] The optimal parameters for the IMT Snake model were $\alpha_1 = 0.2$, $\alpha_2 = 0.2$, $\mu = 1.4$.
[b] The tuned parameters ε and t_m for LDLD were $\varepsilon = 0.2$, $t_m = 0.5$.

$\sigma_1 = 1$ and $\sigma_2 = 15$, and the same curve evolution, the IMT Snake model, for the refinement of their results, where the absolute value of $\frac{\partial f}{\partial y}(x, y)$ was normalized to 0–1 and the sampling interval was 10 pixels. The range of IMT (0.4–1.3 mm), which was obtained through manually measuring the clinical images, determined that $d_{\min} = 6$ and $d_{\max} = 20$ for all the algorithms. For PL-DDP and LDLD, the intra-angular constraint ω_2 relies on the width of the image segment because as $l_{\max}$ increases, S decreases, and the angle between adjacent line segments may increase. We choose $\omega_1 = 0$ to impose parallelism and $\omega_2 = \frac{\pi}{9}$ to enable a relatively large range of selection for $l_{\max}$.

The parameters of the IMT Snake model were vital to the accuracy of the segmentation, so we trained them through minimizing a criterion on the mean of the errors for all the interfaces. To avoid a large time expense relating to the high dimensional parameter space, the training process took a coarse-to-fine (2 scales) scheme by using a step of 0.2 to locate the coarse optimal parameters whose vicinity was searched for fine parameters with a step of 0.1. Similar to this process, the parameters of DDP κ_1, κ_2, PL-DDP $l_{\max}$, and LDLD $l_{\max}$, λ were trained with a step of (0.04, 0.04), 10, and (10, 1), respectively, in both the case with snake refinement and the case without. For LDLD, $l_{\max}$, λ were trained when ε and t_m both took a small value in order not to miss any optimal solution. Then, ε and t_m were increased separately by step 0.1 until the accuracy notably decreased. The remaining parameters were requirements of the implementation so they were tuned heuristically as $\theta_{\min} = 0$, $\theta_{\max} = \frac{\pi}{6}$ for PL-DDP and $\Delta\rho = 1$, $\Delta\theta = \frac{\pi}{45}$, $\theta_\varepsilon = \Delta\theta$, for LDLD. Table 1 shows the trained optimal parameters for the three methods, including with snake refinements and without.

6. Results

Fig. 9 shows segmentation results of these DPs for a synthetic image. We note that all the methods produced satisfactory contours that were close to the boundaries, especially from DDP, PL-DDP with $l_{\max} = 10$ and LDLD with $l_{\max} = 10$. For PL-DDP and LDLD, when the width of the image segment became larger, some unsmooth joints could be generated due to the piecewise linear representation of the boundary curve (see Fig. 9d and f). Although this shortcoming seems unworthy for this simple task of parallel boundary detection, in the later part of this Section, we will see that, for unclear ultrasound artery images, piecewise linear representation is a more robust approach.

Fig. 10 shows the segmentation results of LDLD based on the trained optimal parameters for the typically difficult tasks in Fig. 1. We can see that all the results were good approximations to the boundaries through overcoming noise in the lumen, the missing boundary of LI and the edges in the thick IMC. However, the contours obtained from only LDLD present unsmooth joints. Because the gold standard contours from manual delineation were smooth curves with sub-pixel accuracy (see Fig. 1), discrete optimization methods such as DP might have biased segmentation results to this problem. Nevertheless, if snake refinement was applied on the initial results, then we could expect a more accurate solution.

6.1. Accuracy comparison

Although DDP and PL-DDP were proposed without snake refinement, we also employed snake refinement after their initial detection for a fair comparison of the accuracy among the three methods. Table 2 shows the statistics of their segmentation errors for cases with snake refinement and without. We found that all the methods with snake refinement were better than their counterparts without refinement. This result could be explained by our gold standard that had sub-pixel accuracy, so optimization in the continuous space could be more appropriate. We can also note that, when no snake refinement was applied, the PL-DDP had superior performance compared with the other two methods. This may be attributed to the robust line representation of PL-DDP by two endpoints. However, when snake refinement was introduced, the proposed LDLD performed slightly better than PL-DDP and DDP. Because snake refinement tends to compensate for inaccurate line representation that is sufficiently close to the boundary, the feature of LDLD that allows for adjacent line segments that are connected with disjoints could explain our slightly better performance.

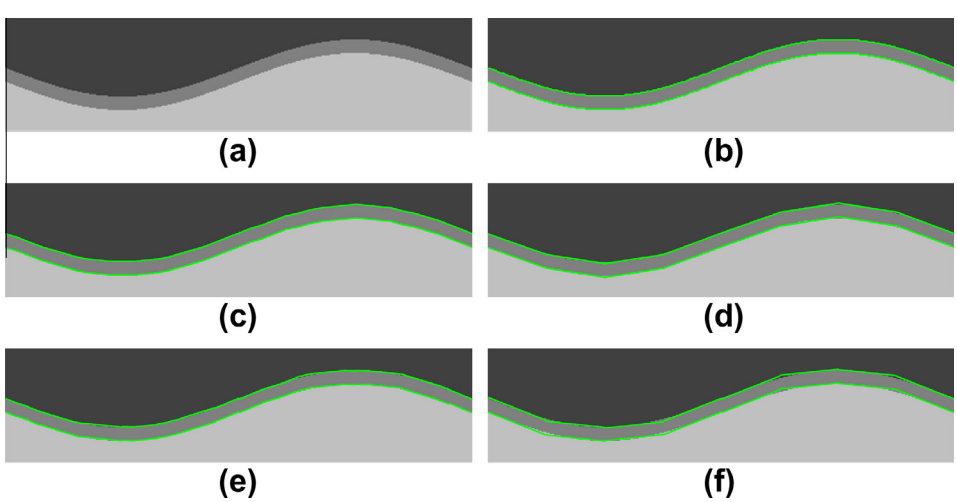

Fig. 9. Segmentation results for an artificial image of size 400 × 100, which contains two boundaries defined by a sinusoid function. (a) Original image. (b) DDP. (c) PL-DDP with $l_{\max} = 10$. (d) PL-DDP with $l_{\max} = 50$. (e) LDLD with $l_{\max} = 10$, $\lambda = 4$. (f) LDLD with $l_{\max} = 50$, $\lambda = 4$.

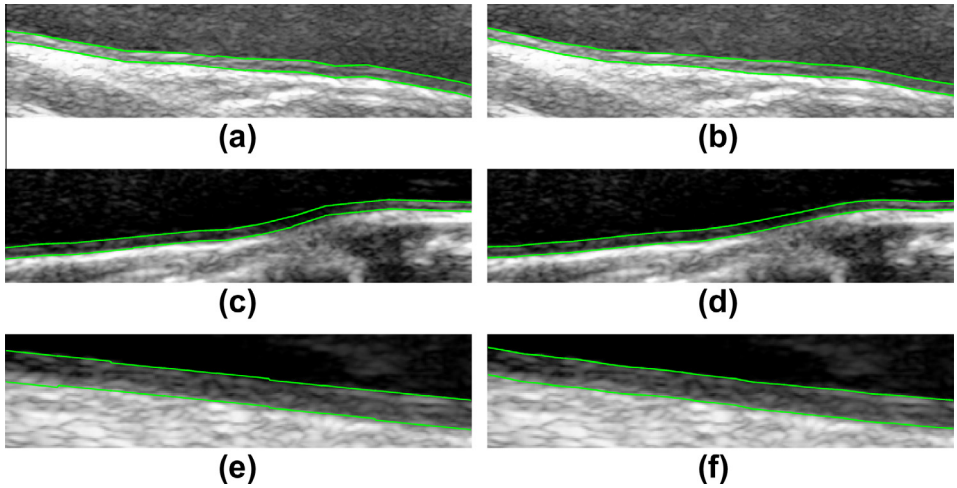

Fig. 10. Segmentation results for the difficult images in Fig. 1. The left column shows the results from LDLD using $l_{max} = 30$, $\lambda = 4$. The right column shows the results of the IMT Snake model on the initial estimation of LDLD using $l_{max} = 60$, $\lambda = 4$.

Table 2
Accuracy comparison among all the methods, including cases with snake refinement and cases without.[a]

MAD (μm)	LI (MeanSD)	MA (MeanSD)	IMC (MeanSD)
Without snake			
DDP	60.8 ± 33.3	54.1 ± 24.3	57.5 ± 25.3
PL-DDP	55.7 ± 28.3	50.1 ± 23.6	52.9 ± 20.3
LDLD	55.2 ± 41.2	53.3 ± 23.5	54.3 ± 28.2
With snake			
DDP	53.7 ± 30.4	45.7 ± 26.0	49.7 ± 24.2
PL-DDP	52.2 ± 29.7	45.6 ± 24.2	48.9 ± 21.9
LDLD	50.0 ± 23.6	45.5 ± 24.6	47.8 ± 20.6

[a] The number of images was 200.

The boundary points of DDP were searched in every column; thus, we can expect it to be more accurate than the methods of piecewise linear approximation. The inferior performance of DDP in Table 2 could be explained by Fig. 11, which uses two examples to illustrate the shortcoming of DDP. We can see that the optimal parameter set failed to detect the boundary at the right end of the left ROI because of strong edges in the adventitia (see Fig. 11c). If we want to overcome this interference, a larger smoothness κ_2 needs to be provided. However, when κ_2 was large enough to guarantee a good segmentation of the left ROI (see Fig. 11e), it failed to detect the boundary in the right ROI due to slanting weak boundary (see Fig. 11f). Note that the two ROIs both feature smooth boundaries, but the boundaries have different slopes. The dilemma that the same smoothness κ_2 could not satisfy them simultaneously suggests that the smoothness measure is not rotation invariant. For piecewise linear approximation, it is not a problem with an appropriate selection for the length of the line

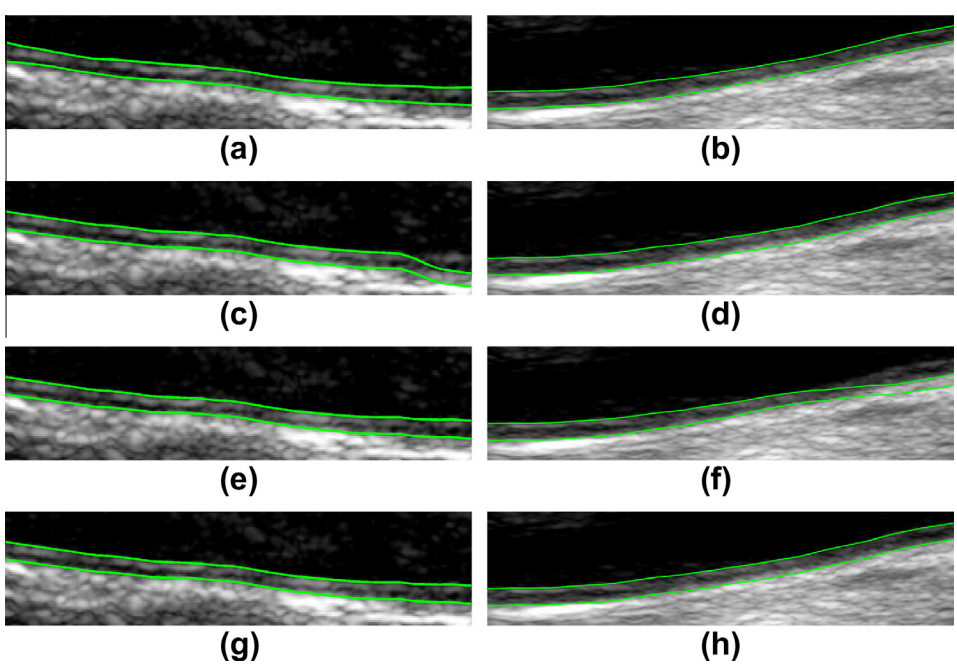

Fig. 11. Two examples illustrating the inferior performance of DDP. (a) (b) Gold standard. (c) (d) DDP using $\kappa_1 = 0.68$, $\kappa_2 = 0.12$. (e) (f) DDP using $\kappa_1 = 0.68$, $\kappa_2 = 0.6$. (g) (h) LDLD using the same set of parameters $l_{max} = 60$, $\lambda = 4$. All the DP generated contours were refined by the IMT Snake model.

Table 3
Efficiency comparison on clinical images among the three methods.

Total time (s)	DDP	PL-DDP	LDLD
Without snake	10.4	104.8	23.0
With snake	10.4	108.7	13.2

segment and the rotation invariant angular constraint between two adjacent line segments (see Fig. 11g and h).

6.2. Efficiency comparison

The efficiency comparison was conducted on clinical images among DDP, PL-DDP and LDLD. Because they employed the same edge map computation and snake refinement to achieve optimal accuracy, we eliminate these two parts while only counting the elapsed time of the two parts of DP, forward recursion and backward tracing, for the efficiency comparison. Table 3 gives the total computation time for all 200 ROIs among the three methods. Although the theoretical complexity of LDLD is $O(N)$, the time costs indicate that the efficiency of LDLD was slightly inferior to DDP but was better than PL-DDP. The less time cost of DDP could be attributed to its simple form of calculation and the lower height of the ROIs.

Fig. 12 shows the time cost with respect to different parameters and image sizes among the three methods. First, we can observe in Fig. 12a that a larger $l_{\max}$ leads to a longer computation time for PL-DDP but a shorter time for LDLD. This phenomenon occurs because as $l_{\max}$ increases, the range of possible $\mathbf{e}_{s-1}$ for computation in PL-DDP increases quadratically while the size of the cost map of LDLD decreases nearly linearly. Although with a small $l_{\max}$, the PL-DDP appears to have a similar time cost compared to LDLD, considering that snake refinement is necessary for an accurate segmentation, which gives the selection of $l_{\max}$ more room, we think the notably superior efficiency of LDLD when $l_{\max}$ is large can be more useful in practice. Then, we can see the efficiency comparison among the three methods for the synthetic image in Fig. 9 with varying sizes (here we test only square images). Note that setting $l_{\max}$ to be too small or too large can bias the efficiency of LDLD or PL-DDP according to Fig. 12a, so we chose a median value $l_{\max} = 50$ for both of them. Fig. 12b indicates that, via computing on the edge points instead of the whole image plane, the speed of LDLD was faster by 2–5 times compared with DDP and faster by 21–81 times compared with PL-DDP on square images of sizes ranging from 100 to 1000 pixels.

Although for our clinical images, the DDP outperformed methods of piecewise linear approximation in terms of the time cost, we note that this advantage vanished as the images became large; moreover, it was accompanied by a large expense in memory. For example, given the average ROI size of 286 × 83 pixels in clinical images, our improved implementation for DDP (see Section 2; otherwise, it would not be applicable for large images) still required at least 2.5 MB ($(M - d_{\min})(d_{\max} - d_{\min} + 1)N$ elements in the cost map), and this situation would become worse as the image became large (114 MB for an image of size 1000 × 1000). In contrast, the memory requirement for LDLD was much smaller because only a small subset of parameters controlling line segments needed to be stored.

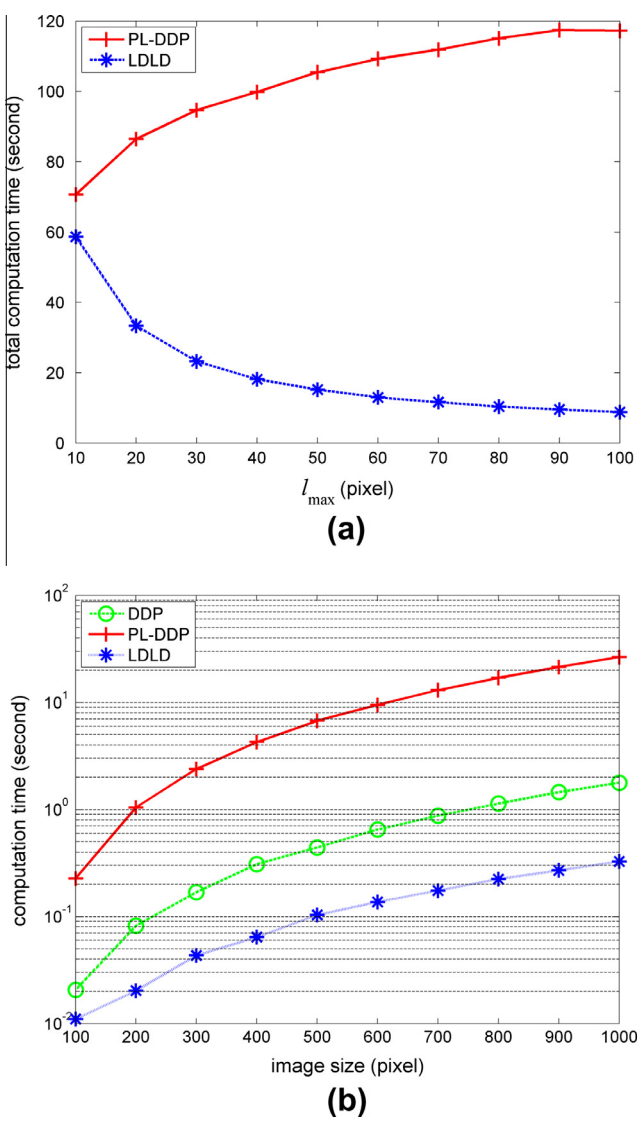

Fig. 12. Efficiency comparison with respect to different parameters and image sizes. (a) Total computation time on clinical images versus $l_{\max}$ between PL-DDP and LDLD. (b) Computation time on synthetic images versus image sizes among the three methods.

6.3. Parameter analysis

Some parameters of LDLD were tuned according to the geometric characteristics of the boundary, e.g., $d_{\min}$, $d_{\max}$, ω_1, ω_2, while some were trained to minimize the overall error, e.g., $l_{\max}$, λ. Here, we consider other types of parameters, which were tuned heuristically as requirements of implementation. For the implementation of CDLD, the choices of $\Delta\rho$ and $\Delta\theta$ control the accuracy of CDLD, and the threshold ε determines the edge points. We set $\Delta\rho = 1$ to make the accuracy of the distance between two line segments to be at the pixel-level, and we chose a large value for $\Delta\theta$ for the sake of efficiency because discretization error can be compensated by

Table 4
Analysis of the accuracy and efficiency with respect to ε.

ε	0.1	0.2	0.3	0.4	0.5	0.6
Overall error (μm)	47.8	47.8	48.3	56.4	66.2	74.1
Total time (s)	16.3	12.8	10.6	9.2	7.8	6.9

Table 5
Analysis of the accuracy and efficiency with respect to t_m.

t_m	0.1	0.2	0.3	0.4	0.5	0.6
Overall error (μm)	47.8	47.8	47.8	47.8	47.8	48.2
Total time (s)	688.0	196.3	69.4	27.2	12.8	8.4

snake refinement. We computed the overall error and the total time cost with respect to different ε in Table 4. It shows that, although the overall error increased when $\varepsilon \geqslant 0.3$, the total time cost was quite stable when the accuracy stayed unchanged, $\varepsilon \leqslant 0.2$.

The DP of LDLD selects optimal line segments from thresholded elements of the sparse matrix, which in fact contains many small non-zero values. We can expect that the parameter for thresholding, t_m, has a large impact on the efficiency of the following DP. Table 5 gives the performance of LDLD with respect to different t_m when snake refinement was used. We can see that, although the complexity of LDLD is $O(N)$ according to Section 3, the DP was still quite slow when this threshold was small. It is also noticeable that, when t_m took values that were equal to or less than 1/2, the overall error with snake refinement stayed unchanged. Suppose that an image segment displays only one side boundary while the other side boundary totally disappears; 1/2 could be a threshold to consider such a situation in the DP if the maximum of the sparse matrix is twice as large as the sum of the strengths of the displayed side boundary.

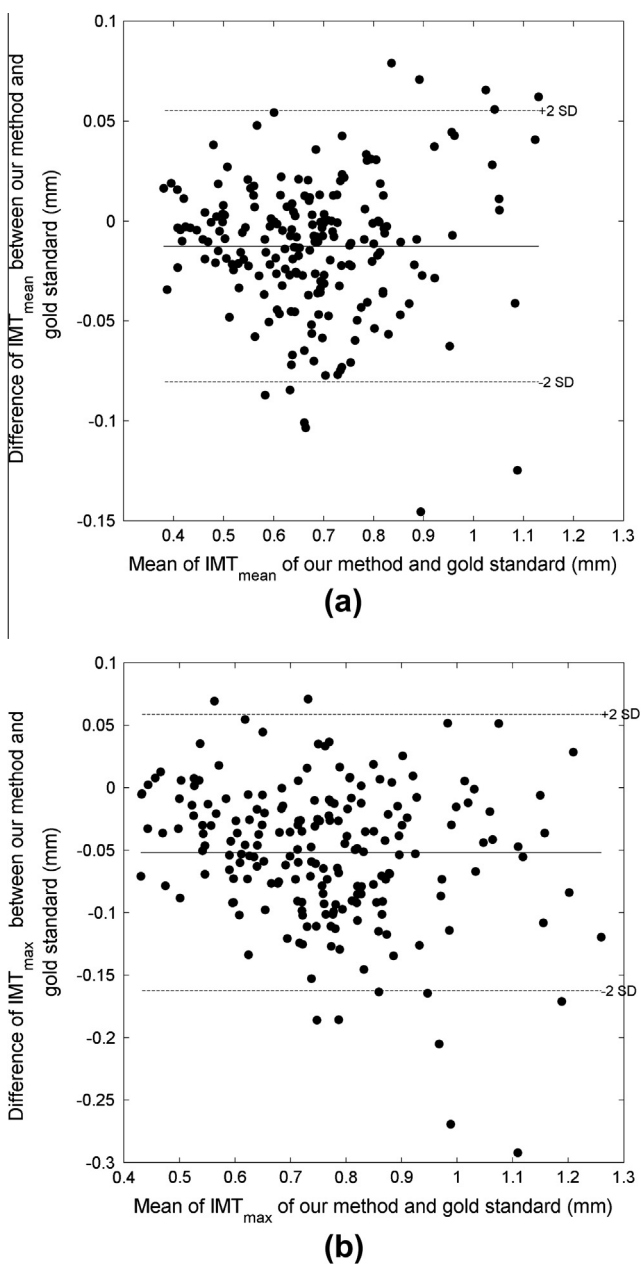

Fig. 13. Bland–Altman plots for mean (a) and maximal (b) IMT between LDLD with snake refinement and the gold standard.

6.4. Statistical evaluation

To evaluate the clinical applicability of the proposed methods, we compared two commonly acknowledged parameters, the mean and the maximal value of IMT, between LDLD with snake refinement and the gold standard. For each pixel column, the thickness was calculated by the vertical distance between two contours and an estimated slope from a fitted smooth curve. For a ROI, the mean and maximal IMT were obtained from the thickness of all the pixel columns. We used the Bland–Altman plot (Bland and Altman, 1986) to evaluate the difference between the two measures. Fig. 13 shows the Bland–Altman plots, where the differences are located in −80.6 to 55.3 μm, −162.6 to 58.9 μm for the mean and maximal IMT, respectively, within a 95% confidence interval. The larger error range of the maximal IMT can be attributed to the large trained parameter $\mu = 1.4$ for the uniform energy in the IMT Snake model, which obliterated the boundary details contributing to maximal IMT. Note that, given a small uniform energy, such details can still be maintained in segmentation contours.

7. Discussion and conclusion

This paper attempts to solve a problem, parallel boundary detection, which emerges in medical imaging applications such as boundary detection on carotid arteries in ultrasound images or the detection of spines in X-ray images. We improved the implementation of two previous methods, DDP and PL-DDP, to render them able to solve the problem in $O(NM)$ complexity. Then, a novel DP based approach, LDLD with rotation invariance and approximately linear time complexity $O(N)$, was proposed to approximate the boundaries using piecewise linear representation. We also embedded the LDLD into a framework for segmentation of intima-media in ultrasound images and validated the method through comparing it with DDP and PL-DDP on a dataset of 200 ROIs. To conclude this paper, we present some final remarks:

1. The cost function of LDLD is very similar to that of DDP and PL-DDP. All of them attempt to find two curves that pass through strong edges as many as possible while satisfying certain hard constraints; however, the form of the solution is quite different so that the edge direction can be used to reduce the computational cost. Moreover, because of the auxiliary edge directions in our solution, the algorithm can selectively detect boundaries of objects with desired patterns.
2. The robustness and accuracy of LDLD rely on an initial piecewise linear approximation and a subsequent snake refinement. The two steps could be a requirement of difficult medical imaging applications according to our experiments. The DDP may directly detect the two side boundaries accurately through imposing further constraints, e.g., a second order derivative, but this could add more parameters for training, and the speed would be hampered.
3. The proposed method is intended only for segmenting nearly parallel boundaries, which may limit its use for plaque. However, because plaque tends to grow into irregular shapes that are difficult to model analytically, few papers have focused on this topic. Actually, according to Fig. 13, we included some pathological cases with IMT > 1 mm, which may be identified as plaque by some clinicians. Although the method in this paper shows an improved accuracy and efficiency to some extent, it also brings some hidden parameters for tuning. This is a

drawback of our method, but we think it is acceptable in clinical applications and, in practice, the selection of parameters is somewhat robust according to Section 6.3.

4. Finally, the LDLD can be extended in several aspects, e.g., changing the linkage from the soft constraint to a hard constraint, detecting two circular parallel boundaries via a polar transform of the original image. Although we apply the proposed LDLD only to intima-media segmentation in this paper, extension to other types of boundaries with edge directions pointing to different sides is intrinsic.

Acknowledgments

This work was partly supported by the Ministry of Science and Technology, China, under the International Cooperation Project (Grant No. 2009DFA12290), when the first author was at Huazhong University of Science and Technology, Wuhan, Hubei, China. The authors thank Linjing Zhou in Zhongnan Hospital for her manual delineation of the intima-media in clinical images and the anonymous reviewers for their comments to improve the paper.

Appendix A. Appendix

The solution of the IMT Snake model is two functions $y_1(x)$ and $y_2(x)$ that satisfy the coupled PDE in (25) and (26)

$$\frac{\partial y_1}{\partial t} = \lambda_1 \frac{\partial^2 y_1}{\partial x^2} - \mu \frac{\partial^2 y_2}{\partial x^2} + \frac{\partial f}{\partial y}(x, y_1)$$
$$\frac{\partial y_2}{\partial t} = \lambda_2 \frac{\partial^2 y_2}{\partial x^2} - \mu \frac{\partial^2 y_1}{\partial x^2} + \frac{\partial f}{\partial y}(x, y_2)$$

where $y_i(x, t)$ denotes the function for contour $\Gamma_i(t)$: $[1, N] \times [0, +\infty) \to [1, M]$. The numerical scheme approximates the space derivative by the centered second difference and the time derivative by a forward difference. For their right-hand side, the implicit difference schemes are applied to the first two terms, and an explicit difference scheme is applied to the third term.

$$\frac{y_{1,j}^{n+1} - y_{1,j}^{n}}{\tau} = \lambda_1 \frac{y_{1,j-1}^{n+1} + y_{1,j+1}^{n+1} - 2y_{1,j}^{n+1}}{h^2} - \mu \frac{y_{2,j-1}^{n+1} + y_{2,j+1}^{n+1} - 2y_{2,j}^{n+1}}{h^2} + f_y\left(x_j, y_{1,j}^{n}\right) \tag{27}$$
$$\frac{y_{2,j}^{n+1} - y_{2,j}^{n}}{\tau} = \lambda_2 \frac{y_{2,j-1}^{n+1} + y_{2,j+1}^{n+1} - 2y_{2,j}^{n+1}}{h^2} - \mu \frac{y_{1,j-1}^{n+1} + y_{1,j+1}^{n+1} - 2y_{1,j}^{n+1}}{h^2} + f_y\left(x_j, y_{2,j}^{n}\right) \tag{28}$$

where $y_{i,j}^n$ is the jth point of y_i at time n, $i = 1, 2, j = 1, 2, \ldots, J$. For simplicity, we set $\tau = 1$, $h = 1$. Note that non-unit τ and h amount to different λ_i μ below and a constant multiplier τ before $f_y\left(x_j, y_{i,j}^n\right)$. Therefore, (27) and (28) become

$$-\lambda_1 y_{1,j-1}^{n+1} + (1 + 2\lambda_1) y_{1,j}^{n+1} - \lambda_1 y_{1,j+1}^{n+1} + \mu y_{2,j-1}^{n+1} - 2\mu y_{2,j}^{n+1} + \mu y_{2,j+1}^{n+1} = y_{1,j}^{n} + f_y\left(x_j, y_{1,j}^{n}\right) \tag{29}$$
$$-\lambda_2 y_{2,j-1}^{n+1} + (1 + 2\lambda_2) y_{2,j}^{n+1} - \lambda_2 y_{2,j+1}^{n+1} + \mu y_{1,j-1}^{n+1} - 2\mu y_{1,j}^{n+1} + \mu y_{1,j+1}^{n+1} = y_{2,j}^{n} + f_y\left(x_j, y_{2,j}^{n}\right) \tag{30}$$

Combining the equations from all the curve points according to (29) and (30), we have

$$\mathbf{A}_1 \mathbf{Y}_1^{n+1} + \mathbf{B}\mathbf{Y}_2^{n+1} = \mathbf{Y}_1^{n} + \mathbf{F}_1^{n} \tag{31}$$
$$\mathbf{A}_2 \mathbf{Y}_2^{n+1} + \mathbf{B}\mathbf{Y}_1^{n+1} = \mathbf{Y}_2^{n} + \mathbf{F}_2^{n} \tag{32}$$

where $\mathbf{Y}_i^n = \left(y_{i,1}^n, y_{i,2}^n, \ldots, y_{i,J}^n\right)^T$, $\mathbf{F}_i^n = \left(f_y\left(x_1, y_{i,1}^n\right), f_y\left(x_2, y_{i,2}^n\right), \ldots, f_y\left(x_J, y_{i,J}^n\right)\right)^T$, $\mathbf{A}_i$ is a tridiagonal matrix of three diagonals $-\lambda_i$, $(1 + 2\lambda_i)$, $-\lambda_i$, and $\mathbf{B}$ is another tridiagonal matrix of three diagonals μ, -2μ, μ. The boundary condition $y_{i,0}^n, y_{i,J+1}^n$, which is calculated by using linear extrapolation for the centers $c_j^n = \frac{1}{2}\left(y_{1,j}^n + y_{2,j}^n\right)$ and mirror reflection for the distances $d_j^n = y_{2,j}^n - y_{1,j}^n$ (see (Xu et al., 2012) for details), modifies the first and last elements in $\mathbf{F}_i^n$ according to (29) and (30). Solving (31) and (32), we obtain the final iteration equations

$$\mathbf{Y}_1^{n+1} = \mathbf{C}_1 \mathbf{Z}_1 - \mathbf{D}_1 \mathbf{Z}_2 \tag{33}$$
$$\mathbf{Y}_2^{n+1} = \mathbf{C}_2 \mathbf{Z}_2 - \mathbf{D}_2 \mathbf{Z}_1 \tag{34}$$

where

$$\mathbf{Z}_1 = \mathbf{Y}_1^n + \mathbf{F}_1^n$$
$$\mathbf{Z}_2 = \mathbf{Y}_2^n + \mathbf{F}_2^n$$
$$\mathbf{C}_1 = \left(\mathbf{A}_1 - \mathbf{B}\mathbf{A}_2^{-1}\mathbf{B}\right)^{-1}$$
$$\mathbf{C}_2 = \left(\mathbf{A}_2 - \mathbf{B}\mathbf{A}_1^{-1}\mathbf{B}\right)^{-1}$$
$$\mathbf{D}_1 = \left(\mathbf{A}_2 \mathbf{B}^{-1} \mathbf{A}_1 - \mathbf{B}\right)^{-1}$$
$$\mathbf{D}_2 = \left(\mathbf{A}_1 \mathbf{B}^{-1} \mathbf{A}_2 - \mathbf{B}\right)^{-1}$$

References

Amini, A., Weymouth, T.E., Jain, R.C., 1990. Using dynamic programming for solving variational problems in vision. IEEE Transactions on Pattern Analysis and Machine Intelligence 12, 855–867.

Ballard, D.H., 1981. Generalizing the Hough transform to detect arbitrary shapes. Pattern Recognition 13, 111–122.

Bao, P., Zhang, L., Wu, X., 2005. Canny edge detection enhancement by scale multiplication. IEEE Transactions on Pattern Analysis and Machine Intelligence 27, 1485–1490.

Bland, J.M., Altman, D.G., 1986. Statistical methods for assessing agreement between two methods of clinical measurement. The Lancet 327, 307–310.

Bots, M.L., Hoes, A.W., Koudstaal, P.J., Hofman, A., Grobbee, D.E., 1997. Common carotid intima-media thickness and risk of stroke and myocardial infarction: the Rotterdam Study. Circulation 96, 1432–1437.

Caselles, V., Kimmel, R., Sapiro, G., 1997. Geodesic active contours. International Journal of Computer Vision 22, 61–79.

Chen, Y., Tagare, H.D., Thiruvenkadam, S., Huang, F., Wilson, D., Gopinath, K.S., Briggs, R.W., Geiser, E.A., 2002. Using prior shapes in geometric active contours

in a variational framework. International Journal of Computer Vision 50, 315–328.
Cheng, D., Schmidt-Trucks ss, A., Cheng, K., Burkhardt, H., 2002. Using snakes to detect the intimal and adventitial layers of the common carotid artery wall in sonographic images. Computer Methods and Programs in Biomedicine 67, 27–37.
Cheng, D.C., Jiang, X., 2008. Detections of arterial wall in sonographic artery images using dual dynamic programming. IEEE Transactions on Information Technology in Biomedicine 12, 792–799.
Deans, S.R., 1981. Hough transform from the Radon transform. IEEE Transactions on Pattern Analysis and Machine Intelligence, 185–188.
Destrempes, F., Meunier, J., Giroux, M.F., Soulez, G., Cloutier, G., 2009. Segmentation in ultrasonic B-mode images of healthy carotid arteries using mixtures of Nakagami distributions and stochastic optimization. IEEE Transactions on Medical Imaging 28, 215–229.
Duda, R.O., Hart, P.E., 1972. Use the Hough transformation to detect lines and curves in pictures. Communications of the ACM 15, 11–15.
Kass, M., Witkin, A., Terzopoulos, D., 1988. Snakes: active contour models. International Journal of Computer Vision 1, 321–331.
Lamont, D., Parker, L., White, M., Unwin, N., Bennett, S., Cohen, M., Richardson, D., Dickinson, H.O., Adamson, A., Alberti, K., 2000. Risk of cardiovascular disease measured by carotid intima-media thickness at age 49–51: lifecourse study. British Medical Journal 320, 273–278.
Liang, Q., Wendelhag, I., Wikstrand, J., Gustavsson, T., 2000. A multiscale dynamic programming procedure for boundary detection in ultrasonic artery images. IEEE Transactions on Medical Imaging 19, 127–142.
Loizou, C.P., Pattichis, C.S., Pantziaris, M., Tyllis, T., Nicolaides, A., 2007. Snakes based segmentation of the common carotid artery intima media. Medical and Biological Engineering and Computing 45, 35–49.
Molinari, F., Zeng, G., Suri, J.S., 2010. A state of the art review on intima-media thickness (IMT) measurement and wall segmentation techniques for carotid ultrasound. Computer Methods and Programs in Biomedicine 100, 201–221.
Noble, J.A., Boukerroui, D., 2006. Ultrasound image segmentation: a survey. IEEE Transactions on Medical Imaging 25, 987–1010.
O'Leary, D.H., Polak, J.F., Kronmal, R.A., Manolio, T.A., Burke, G.L., Wolfson, S.K., 1999. Carotid-artery intima and media thickness as a risk factor for myocardial infarction and stroke in older adults. The New England Journal of Medicine 340, 14–22.
Poredos, P., 2004. Intima-media thickness: indicator of cardiovascular risk and measure of the extent of atherosclerosis. Vascular Medicine 9, 46–54.
Rocha, R., Campilho, A., Silva, J., Azevedo, E., Santos, R., 2010. Segmentation of the carotid intima-media region in B-mode ultrasound images. Image and Vision Computing 28, 614–625.
Rocha, R., Campilho, A., Silva, J., Azevedo, E., Santos, R., 2011. Segmentation of ultrasound images of the carotid using RANSAC and cubic splines. Computer Methods and Programs in Biomedicine 101, 94–106.
Rosenfeld, A., 1970. A nonlinear edge detection technique. In: Proceedings of the IEEE, pp. 814–816.
Spall, J., 2003. Introduction to Stochastic Search and Optimization: Estimation, Simulation, and Control. John Wiley and Sons.
Sun, C., Appleton, B., 2005. Multiple paths extraction in images using a constrained expanded trellis. IEEE Transactions on Pattern Analysis and Machine Intelligence 27, 1923–1933.
Sun, C., Vallotton, P., Wang, D., Lopez, J., Ng, Y., James, D., 2009. Membrane boundary extraction using circular multiple paths. Pattern Recognition 42, 523–530.
Toronto, N., Morse, B.S., Ventura, D., Seppi, K., 2007. The Hough transform's implicit Bayesian foundation. In: IEEE International Conference on Image Processing, pp. 377–380.
Wei, G.-Q., Qian, J., Schramm, H., 2001a. A dual dynamic programming approach to the detection of spine boundaries. In: Niessen, W., Viergever, M. (Eds.), Medical Image Computing and Computer-Assisted Intervention – MICCAI 2001. Springer, Berlin/Heidelberg, pp. 524–531.
Wei, G.-Q., Qian, J., Schramm, H., 2001b. Generalized dynamic programming approaches for object detection: detecting spine boundaries and vertebra endplates. In: Proceedings of the 2001 IEEE Computer Society Conference on Computer Vision and Pattern Recognition (CVPR 2001), pp. 954–959.
Wendelhag, I., Liang, Q., Gustavsson, T., Wikstrand, J., 1997. A new automated computerized analyzing system simplifies readings and reduces the variability in ultrasound measurement of intima-media thickness. Stroke 28, 2195–2200.
Xie, J., Jiang, Y., Tsui, H., 2005. Segmentation of kidney from ultrasound images based on texture and shape priors. IEEE Transactions on Medical Imaging 24, 45–57.
Xu, X., Zhou, Y., Cheng, X., Song, E., Li, G., 2012. Ultrasound intima-media segmentation using Hough transform and dual snake model. Computerized Medical Imaging and Graphics 36, 248–258.